Final version published as: "The Influence of Electrochemical Aging on Bead-Blasted Nickel Electrodes for the Oxygen Evolution Reaction," Taylor, A. K.; Pauls, A. L.; Paul, M. T. Y.; Gates, B. D., *ACS Applied Energy Materials*, 2019, 2 (5), 3166-3178. DOI: 10.1021/acsaem.8b02224

# The Influence of Electrochemical Aging on Bead-Blasted Nickel Electrodes for the Oxygen Evolution Reaction

*Audrey K. Taylor, Alexi L. Pauls, Michael T. Y. Paul, and Byron D. Gates* *

Department of Chemistry
Simon Fraser University
8888 University Drive
Burnaby, BC V5A 1S6 (Canada)
Telephone Number: (778) 782-8066
Fax Number: (778) 782-3765
Email Address: *bgates@sfu.ca

**ABSTRACT**

The oxygen evolution reaction (OER) is of importance to both electrochemical energy conversion and energy storage. Low-cost, non-precious metal electrocatalysts that can withstand high operational current densities will likely be the best candidates for meeting the commercial needs for a range of OER applications. In addition to electrode composition, the surface morphology of gas evolving electrodes can affect their efficiency and performance. In this work, we demonstrate the influence of electrochemical aging on the performance of micro- and nanoscale textures for the OER. A series of textured Ni electrodes were prepared by rapid, scalable techniques, which included the use of bead-blasting. Two distinct approaches to induce the formation of the active Ni (oxy)hydroxide phase were conducted by electrochemical aging using cyclic voltammetry (CV) methods. The influence of the aging technique was assessed and correlated to the performance of these surface textures. Differences in the morphology of these textures and their resulting surface areas were estimated using three-dimensional (3D) reconstructions obtained from electron microscopy analyses. Focused ion beam (FIB) milling was also performed on the bead-blasted electrodes to visualize buried cracks and voids. The potential required for the OER at an applied current density of 500 $mA/cm^2$ exhibited a reduction of 0.7 V for the electrodes aged by the steady-state treatment. The OER performance of the textured electrodes were found to correlate to both the electrode surface morphology and the type of electrochemical aging applied to the electrodes.

**KEYWORDS:** nickel, textured electrodes, oxygen evolution reaction, bead-blasting, electrochemical aging, alkaline electrolysis

## 1. INTRODUCTION

The oxygen evolution reaction (OER) is a fundamental electrochemical process of significance for its applicability to fuel cells,[1] metal-air batteries,[2] and water electrolyzers.[3] Water electrolyzers, for example, could assist in the clean production of hydrogen, which could help meet demands for energy storage. Excellent materials for commercial, large-scale electrolyzers are low-cost, non-precious metals that can withstand high operational current densities.[4] Nickel-based electrocatalysts have relatively low overpotentials towards the OER under alkaline conditions and can achieve high current densities.[5] Under the applied potentials for the OER, nickel (Ni) can undergo electrochemical oxidation to a β-$Ni(OH)_2$ form and further oxidation to the OER active, β-NiOOH phase.[6] This oxidation from β-$Ni(OH)_2$ to β-NiOOH is often concurrent with a rearrangement into layered, sheet-like structures.[7-9] This electrochemical oxidation of Ni induces a structural rearrangement that can allow for the intercalation of water molecules and possibly ionic impurities such as carbonate species.[10, 11] Activated Ni electrodes with a stable β-NiOOH phase have shown improved efficiency for several electrochemical processes, such as the OER, the hydrogen evolution reaction (HER), and the hydrogen oxidation reaction (HOR).[7, 12-14] The kinetics of the HOR and the HER have been studied experimentally using Ni hydroxide species.[13] The presence of oxide species on the surfaces of the Ni electrodes during the HOR and the HER were found to decrease adsorption energies of the hydrogen atoms, which resulted in reduced activation energies and faster reaction kinetics.[12, 13] Other reports have demonstrated the preparation of activated Ni-based electrocatalysts by the inclusion of alkali-metal cations (e.g., K, Cs).[15] In this prior example, the authors reported the preparation of a relatively thick layer containing a NiOOH phase, which formed a three-dimensional (3D) network with nanoscale features and intercalated cations through cycling the applied potential under conditions of a mild

pH and a high temperature. Improvements to the kinetics of the OER were demonstrated by these activated, high surface area, Ni-based electrodes. In general, the relative amount of the β-NiOOH phase per a given area of the electrode will dictate its performance for electrocatalytic, gas evolving processes such as the HER and the OER.

There are numerous methods to synthesize Ni hydroxide electrocatalysts, but achieving both the desired chemical and physical properties in scalable quantities can be difficult. Non-synthetic routes, such as "electrochemical aging", can induce the formation of the active β-NiOOH phase over relatively large electrode areas.[15, 16] An aged electrode can exhibit a reduction to the overpotential by 60 mV and a 10 fold increase in the rate of the OER.[7] This electrochemical aging can be conducted by consecutive scanning of the potential using cyclic voltammetry (CV) techniques. Repeated scanning of the potential from 0 to 0.6 V (vs Hg/HgO) will initiate the processes associated with the conversion of β-$Ni(OH)_2$ to β-NiOOH. This reversible transformation can be monitored through the associated anodic and cathodic peaks. With each successive CV scan, the anodic and cathodic peaks grow in their intensity, which signifies the growth of the active, β-NiOOH phase.[17] This growth process continues until reaching a thermodynamic equilibrium where the active phase is assumed to be relatively uniform across all of the surfaces of the electrode. At this stage, the anodic and cathodic peaks will be stable and no longer changing with subsequent CV scans.[18, 19] As expected, highly textured electrodes require prolonged electrochemical aging relative to planar electrodes surfaces with less electrochemically active surface area ($A_{ecsa}$). It is essential to assess the OER performance of textured electrodes only after sufficient electrochemical aging when evaluating these materials for industrial applications.

Methods of rapidly producing electrodes with a high $A_{ecsa}$ in a scalable fashion are desired by many industries. The commercial application of water electrolysis requires scalable techniques

that are capable of preparing large (>10 $cm^2$) working electrodes with a high $A_{ecsa}$ (e.g., a roughened texture).[20-22] Microscale textures are often more easily prepared over large areas and at faster rates than nanoscale textures.[23] Although the wetting properties of microscale textures are less well-studied, these textures have demonstrated enhanced gas evolution dynamics (e.g., bubble nucleation, coalescence, and release events).[24-26] In addition, there are only a few reported examples that evaluate the efficiency of gas evolution reactions for microstructures prepared over large areas.[22, 27, 28] Electrodeposition is a widely used technique that can produce microscale textures over large areas.[20, 29, 30] For example, Ni-based electrodes were prepared by electrodeposition techniques to produce cauliflower-like microspheres (10-μm in diameter and 20-μm in thickness) for the HER.[29, 31] These electrodeposited textures exhibited good durability and remained active towards the HER in 30 wt % KOH over a period of 3 months.[29] Porous 3D Ni foams have been prepared by hydrogen bubble templating at high cathodic current densities.[32] The microscale pores within the 3D foam have typical diameters ranging from 120 to 220 μm. It has been proposed in previous work that these relatively large microscale pores can enable a faster dissipation of gas bubbles from the electrode surfaces.[33] Microscale textures on the surfaces of electrodes, if not accomplished by electrodeposition techniques, are typically achieved by post-processing methods. For example, mechanical roughening by abrasion of electrode surfaces has been widely used in the water electrolysis industry.[34] Another simple and scalable approach to prepare microscale textures on electrodes is bead-blasting. Bead-blasting is an industrial process capable of quickly treating large substrates. This process could be used to create textures on electrodes composed of earth-abundant materials, such as the first row transition metals (e.g., Ni, Fe, Mn, and Co). Microscale textures on these electrodes, prepared by these scalable processes, could be useful for a range of gas evolution reactions including the OER.

In this work, two distinct approaches to electrochemical aging were compared for their influence on the OER activity for a series of textured Ni electrodes. Microscale textures were prepared on Ni electrodes by a bead-blasting technique. This technique was chosen as a simple, scalable approach to achieve a microscale roughness. Electrodes with nanoscale textures were prepared by the electrodeposition of Ni onto planar, polished Ni surfaces. Planar Ni electrodes, without any surface texture, were prepared by polishing polycrystalline Ni rods. The effects of electrochemical aging under alkaline conditions were correlated to the performance of these distinct surface textures towards gas evolution during the OER. Electrochemical aging of each type of Ni electrode was conducted by CV methods using either a "limited aging" or a "steady-state" aging technique. The limited aging technique applied a pre-determined number of CV scans, while the steady-state aging technique applied a sufficient number of CV scans to achieve stabilization of the β-NiOOH phase. Stabilization of the electrochemically formed β-NiOOH phase was indicated by the character of the electrochemical transformations between Ni (II) and Ni (III) in the CV profiles. The surface area values ($SA_f$) of the textured surfaces were estimated from 3D surface reconstructions obtained by stereo-view imaging using scanning electron microscopy (SEM) techniques. Focused ion beam (FIB) milling was also performed on the bead-blasted electrodes to visualize voids beneath their surfaces that formed during the texturing process. The elemental composition of the bead-blasted surfaces were further analyzed by Auger electron spectroscopy (AES). Following the electrochemical aging of the Ni electrodes, their electrochemical performance towards the OER was assessed by techniques that included linear sweep voltammetry (LSV), chronopotentiometry (CP), and chronoamperometry (CA) measurements.

## 2. EXPERIMENTAL SECTION

### *2.1 Materials and Reagents*

High purity Ni rods (99.9998%) with a diameter of 6.35 mm were purchased from Sigma Aldrich and cut into sections 8 mm in length for use as the working electrodes. Nickel nitrate hexahydrate [$Ni(NO_3)_2$•$6H_2O$, Sigma Aldrich, 99.999%, CAS no. 13478-00-7], sodium dodecyl sulfate (SDS, Sigma Aldrich; ≥98.5%, Lot no. 098K0160), nickel sulfate hexahydrate ($NiSO_4$•$6H_2O$ Sigma Aldrich, 99.999%, CAS no. 10101-97-0), hydrogen peroxide ($H_2O_2$, Fisher Scientific, 30% v/v in water, CAS no. 7722-84-1), sulfuric acid ($H_2SO_4$, Caledon Chemicals, CAS no. 7664-93-9), boric acid ($H_3BO_3$, Sigma Aldrich; 99.999% CAS no. 10043-35-3), acetone (Fisher Scientific, reagent grade, CAS no. 67-64-1), isopropyl alcohol (IPA, Fisher Chemical, CAS no. 67-63-0), nitric acid ($HNO_3$, Anachemia, 70% v/v in water, CAS no. 7697-37-2), and hydrochloric acid (HCl, ACP Chemicals, 37% v/v in water, CAS no. 7647-01-0) were all used as received from the distributors. Potassium hydroxide pellets (KOH, Semiconductor Grade; 99.99%, CAS no. 1310-58-3) were used to prepare the electrolyte, which was treated by a purification process (see the Electrochemical Measurements section below for details). All aqueous solutions were prepared using high purity water obtained with an in-house filtration system (DI water, 18 MΩ•cm, Barnstead Nanopure DIamond). Polishing of the Ni electrodes was achieved using a Buehler EcoMet 250 equipped with an AutoMet power head. Polishing materials consisted of 30-μm diameter particles on a polishing disc (Buehler; Diamond Disc, Item no. 415408), and a series of cloth discs (Buehler; UltraPad, Item no. 40718) each dedicated for use with different types of the diamond pastes (Buehler; MetaDi Supreme Polycrystalline Diamond Suspensions). The diamond pastes were mixed with a lubricant (Buehler; MetaDi Fluid, Item no. 406032) to prepare a series of suspensions containing the 9, 6, 3, 1, or 0.3-μm diameter particles. The polishing steps

were performed in order of a descending particle size with ample rinsing (~10 mL) of the sample holder when changing from one polishing medium to another. The final polishing paste was an alumina slurry ($Al_2O_3$, Allied High Tech; Micropolish 0.05-μm diameter particle suspension) used with a ChemoMet polishing pad (Buehler; Item no. 424008). Cleaning of the polished and bead-blasted materials was conducted by sonicating each substrate in a series of wash solutions. These wash solutions were acetone, IPA, and DI water, which were each agitated for 20 min using a Branson 1510 sonicator operating at 130 W.

*2.2 Preparation of the Ni Working Electrodes*

The sequence of steps for the preparation of the bead-blasted Ni electrodes involved: (i) polishing to achieve consistently smooth surfaces; (ii) cleaning by sonicating the polished electrodes; (iii) electrodeposition of a high purity Ni base layer onto the polished surfaces; (iv) texturing both the polished and electrodeposited Ni surfaces through a bead-blasting process using pressurized glass beads; and (v) a final cleaning of the bead-blasted electrodes using a sonication technique.

*2.3 Polishing of the Ni Working Electrodes*

The surfaces of the Ni working electrodes were polished to attain a mirror-like finish through a series of steps. Each polishing step had a dedicated cloth and paste. The force applied to the polishing head was 2 lb, and the rotational speed of the base and head were 30 and 230 rpm, respectively. The same force and rotational speeds were used for each of the steps. These pastes had nominal colloidal diameters of 9, 6, 3, 1, 0.3, and 0.05 μm, which were used in order of descending size. Between each of the polishing steps the samples were rinsed with DI water to

prevent cross-contamination of the pastes. After the final polishing step, the Ni electrodes were removed from the custom holder and rinsed with ~20 mL of DI water. These rinsed electrodes were immersed in a separate solution of DI water for 10 min to assist in removing additional residue that may have remained from the polishing process. Each of the samples were successively sonicated for 20 min in acetone, IPA, and DI water (each at a volume of ~100 mL) to further remove polishing residue. After removal of the residual polishing media, the polished Ni stubs were used as working electrodes in the electrochemical experiments outlined below. Several of the polished Ni working electrodes were also processed to achieve a unique surface roughness through the electrodeposition of Ni and/or the bead-blasting of these surfaces.

*2.4 Electrodeposition of Ni onto the Polished Ni Electrodes*

Pre-cleaning of the glassware involved a 20 min soak in piranha followed by a DI water rinse. The glassware was soaked for another 20 min in aqua-regia, and rinsed with an excess of DI water. (*CAUTION! Piranha and aqua-regia are extremely corrosive and care should be taken when handling these reagents.*) The piranha solution was prepared by combining $H_2SO_4$ and 30% $H_2O_2$ in a 3:1 (v/v) ratio. The aqua regia solution was similarly prepared by combining HCl and $HNO_3$ in a 3:1 (v/v) ratio. Clean, dedicated glassware were used to separately prepare both the piranha and aqua regia solutions.

High purity baths of Ni salts were electroplated onto the polished surfaces of the Ni stubs. The Ni plating bath was prepared in a pre-cleaned 250 mL volumetric flask. The plating solution contained $NiSO_4$ (1.8 M), $H_3BO_3$ (0.2 M), and SDS ($3.5 \times 10^{-4}$ M) dissolved in DI water. The plating bath was stirred at 250 rpm for at least one week prior to carrying out the electroplating process to attain a complete dissolution of the reagents. The process of Ni electrodeposition was

conducted using a chronoamperometric setup with a three-electrode configuration. A saturated calomel reference electrode (SCE), a Pt wire (Alfa Aesar, 99.9%) counter electrode, and a polished Ni working electrode were each immersed in the plating solution. The Ni working electrode was positioned in a face-down configuration and jacketed within a Teflon® shroud to prevent electrodeposition on the sides of the electrode. A constant potential of −1.0 V (vs SCE) was maintained for a duration of 10 min while stirring the solution at 870 rpm to aid in the removal of $H_2$ bubbles.[35] After the electrodeposition process, the Ni working electrode was removed from the solution, rinsed with ~3 to 5 mL of DI water, and dried with a filtered stream of $N_2$ gas (Praxair, 99.998%). These electrodeposited Ni electrodes were stored in a clean hood (Microzone Fan Filter Clean Hood, Model VLF-2-4) until performing the subsequent electrochemical measurements. Several of these samples were further processed by bead-blasting to create a textured surface finish.

*2.5 Bead-Blasting of the Ni Electrodes*

Bead-blasting was performed on both the electrodeposited Ni and the as-polished Ni samples to assess the possible impact of the base material (i.e., electrodeposited or polished Ni) on their electrochemical aging and performance. Dry, abrasive bead-blasting was performed using both a Kelco pressurized syphon blasting machine (Model CS-36C) and crushed glass (Enviro-Grit; Stock no. 71106, grit 12/50). Each Ni electrode was treated by bead-blasting for 5 s at a direction normal to the Ni surfaces until achieving a frosty, lustrous appearance. The bead-blasted surfaces were cleaned under a stream of compressed $N_2$ gas (Praxair; 99.998%) followed by sonication in IPA for 20 min. These electrodes were subsequently sonicated in DI water for another 20 min to remove residual bead-blasting materials from their surfaces. After this cleaning process,

the bead-blasted electrodes were stored in covered petri-dishes, which were placed within a clean hood until performing the electrochemical measurements.

*2.6 Electrochemical Measurements of the Ni Electrodes under an Applied Shear Flow*

Rotating disk electrode (RDE) measurements were acquired using a Biologic Science Instruments SP-150 potentiostat and a Modulated Speed Rotator from Pine Research Instrumentation. EC-Lab software was used to record the electrochemical data from the RDE measurements. A custom-built, five-neck glass electrochemical cell was setup with a Hg/HgO reference electrode (SnowHouse Solutions; Model R-XR400) filled with purified 1 M KOH, a graphite counter electrode (Alfa Aesar; 99.9995%, 6.1-mm diameter), and a Ni working electrode. All electrochemical measurements were acquired at 25 ± 0.2 $^{o}$C, maintained using a temperature controlled water bath (Thermo Scientific; Precision 280 Series). The high purity 1 M KOH electrolyte was purified according to a protocol reported by Klaus *et al.* and stored in $N_2$ gas (Praxair; 99.999%) purged plastic bottles until use.[36] The electrolyte was also purged for at least 30 min prior to the start of any electrochemical measurements, and a headspace of $N_2$ gas was maintained throughout the duration of these electrochemical measurements.

Two types of processes were used for the electrochemical aging of the Ni electrodes. These processes were performed by CV techniques prior to assessing each electrode for the OER. The first type of electrochemical aging process is referred to herein as “steady-state aging”, which was administered until the anodic peaks overlapped with a variability of at most 10 μA between 10 consecutive CV scans. Stable anodic peaks in the CV scans indicated that the Ni (oxy)hydroxide phase was no longer changing with respect to further changes in the applied potential. The performance of these Ni electrodes for the OER were only evaluated after the phases of Ni present

on their surfaces had become stable as assessed by the described anodic peak metric. To achieve a stable and consistent β-$Ni(OH)_2$/β-NiOOH phase, many more CV scans (i.e., ~7200 scans) were required by the electrodes with a larger $SA_f$ (i.e., the bead-blasted Ni electrodes). The electrodeposited and polished Ni electrodes required ~70 and ~80 CV scans, respectively, to achieve the same anodic peak stability. Since this response to the steady-state aging process was dramatically different for electrodes with a relatively high $SA_f$ in contrast to those with a significantly lower $SA_f$, the effects of electrochemical aging were also evaluated using a fixed number of CV scans. This second type of electrochemical aging is referred to herein as the "limited aging" process. This process was carried out by applying exactly 100 CV scans to each electrode regardless of the anodic peak stability prior to obtaining the OER measurements. These two types of aging processes were each performed at a scan rate of 100 mV/s, and the applied potential was scanned between 0.0 and 0.6 V (vs Hg/HgO).

A series of LSV experiments were performed immediately after the electrochemical aging. During these LSV experiments each electrode was rotated at a series of set speeds (i.e., 0, 500, 1000, 2000, 3000, and 7000 rpm). The LSV data was obtained by scanning the potential between 0 and 1.2 V (vs Hg/HgO) at a scan rate of 1 mV/s. After conducting each LSV experiment at a specific rotational speed, the working electrode was rotated at 8000 rpm for a period of 5 s to remove $O_2$ bubbles adhered to its surfaces. Prior to the start of each subsequent LSV experiment, five consecutive CV scans were performed at a scan rate of 100 mV/s between the potentials of 0.0 and 0.6 V (vs Hg/HgO). These five CVs were conducted to reform the β-$Ni(OH)_2$ and β-NiOOH phases.

Following the series of LSV measurements, CP was performed for each electrode at a current density of 500 $mA/cm^2$. A low and high rotational speed of 500 and 3000 rpm, respectively,

were sequentially applied during the CP experiments. Relatively high current densities for CP were applied to the samples to mimic industrially relevant conditions, and to evaluate the effects of bubble dynamics as a function of surface texture and electrochemical aging on their overall activity towards the OER. Chronoamperometry (CA) was also performed on each electrode. The electrodes were held at 1.0 V for 7 min during the CA measurements while being rotated at 500, 1000, 2000, 3000, or 7000 rpm. Directly after each CP and CA experiment (e.g., measurements obtained at one rotational speed), the working electrode was rotated at 8000 rpm for 5 s to dislodge $O_2$ bubbles from their surfaces. A duration of 7 min was chosen for both the CP and CA experiments since the electrochemical response of the samples stabilized within this timeframe. The sampling frequency for the CP and CA experiments was set to 0.1 s, and a 50 Hz low pass filter was applied to remove external noise from the data.

*2.7 Stationary Electrochemical Measurements of the Ni Electrodes*

The stationary measurements (e.g., without rotation of the working electrode) were performed in a custom-built, acrylic electrochemical cell using a purified 1 M KOH electrolyte. The electrolyte was purged with $N_2$ gas (Praxair; 99.999%) for 30 min prior to the start of the measurements, and a headspace of the same gas was maintained throughout the duration of the stationary measurements. The reference and counter electrodes (e.g., Hg/HgO and high purity graphite rod, respectively) were consistent with those used for the measurements under the applied shear flow (i.e., while rotated). The working Ni electrode was shrouded by a Teflon® holder and held in a face-up orientation. Steady-state aging was performed using the same methods described above for the RDE study. A slightly lower value for the maximum applied potential was chosen to avoid an overlap with the OER region during the aging process for the stationary measurements.

This aging was performed by CV techniques while scanning the potential from 0 to 0.55 V (vs Hg/HgO). The reason for this adjustment to the upper potential was to avoid the possible accumulation of bubbles at the onset of the OER. A steady-state electrochemical aging method was chosen to convert all of the additional surface area gained by bead-blasting process into the active, β-NiOOH phase. After this aging process, the stabilization of the anodic peak within the CV profile indicated that the β-NiOOH phase was no longer changing with further electrochemical treatment. Consequently, it was inferred that each of the aged electrodes had the same proportion of active layer per the accessible $SA_f$ regardless of the electrode morphology.

Directly after the steady-state electrochemical aging process, a single LSV experiment was performed at a scan rate of 1 mV/s from 0 to 2.0 V (vs Hg/HgO) to probe the dynamics of the OER. The CP and CA experiments were each subsequently performed for a duration of 15 min while holding the working electrode at either 500 $mA/cm^2$ or 1.5 V (vs Hg/HgO), respectively. A higher potential was used for the CA measurement than in the previous RDE measurements to probe higher current densities and, therefore, to induce a higher reaction rate for the OER. The relatively high current densities and high overpotentials for the OER were probed for their relevance to the commercial requirements for this reaction.[21]

*2.8 Characterization of the Surface Features on the Ni Electrodes*

A series of SEM analyses were performed on the samples using an FEI Helios NanoLab 650 SEM/FIB dual beam system. The acceleration voltage was held at 2 kV in a secondary electron detection (SED) mode for the characterization of the polished Ni samples, and at 10 kV for the characterization of all the other Ni samples. The Ni samples were threaded onto custom Al mounts to prevent movement while imaging the samples. The surface morphologies were analyzed by

obtaining images at a 0° and a 15° tilt of each sample. These images were used to reconstruct a 3D representation of the surfaces using MountainsMap® Premium software by Digital Surf (version: 7.4.8270). A smoothing filter of 5 pixels was used during reconstruction of the stereo-pair images. The total area of the reconstructed 3D surfaces was normalized against a 2D projection of the region of interest (i.e., the geometric surface area) to obtain a local surface roughness factor ($R_f$).

A focused Ga ion beam (FIB; Tomahawk™ ion column) on the Helios SEM system was used for milling the samples to reveal cross-sectional features of the bead-blasted electrodes. An acceleration voltage of 30 kV was used to perform the FIB milling processes. These cross-sections enabled a visualization of buried voids beneath the electrode surfaces, which were generated while bead-blasting the Ni electrodes using glass beads.

Auger electron spectroscopy (AES) was performed on the cleaned, bead-blasted surfaces to assess whether impurities had been incorporated into the Ni surfaces during the bead-blasting process. A Kratos Analytical Axis Ultra system was operated in a crossover mode using a field emission electron gun. Five separate locations on each bead-blasted Ni electrode were randomly selected for analysis at an acceleration voltage of 10 kV and a spot size of $6.4 \times 10^3$ $\mu m^2$. This spot size was chosen to survey a relatively large area of the electrode surfaces. Survey scans of the samples were acquired from 480 to 900 eV with a resolution of 0.2 eV and a dwell time of 300 ms.

X-ray photoelectron spectroscopy (XPS) was conducted on pristine electrodeposited and polished Ni surfaces. A bead-blasted surface was also analyzed directly after the steady-state electrochemical aging treatment. This bead-blasted electrode was removed from the electrochemical cell and immediately rinsed with DI water (~20 mL) followed by drying under a $N_2$ gas stream. The aged sample was quickly placed under high vacuum in the XPS system. These

analyses were performed using a Kratos Axis Ultra system. The system contained a monochromatic Al Kα source and DLD detector. High resolution scans were performed on the Ni 2p regions for each sample. All measurements were acquired from 850 to 884 eV with a step size of 0.1 eV, a dwell time of 500 ms, and a pass energy of 20 eV. Any peak shifts were corrected to the adventitious C 1s peak at 284.8 eV.

## 3. RESULTS AND DISCUSSION

### *3.1 Characterization of the Ni Electrode Morphology by Scanning Electron Microscopy*

A series of Ni electrodes with micro- and nanoscale textures were prepared using scalable methods to correlate both surface textures and electrochemical aging techniques to their resulting performance towards the OER. To create the microscale textures, two different types of electrode surfaces were subjected to bead-blasting. These two types of bead-blasted electrodes are referred to as BB-edep and BB-pol, which indicates the presence of either an electrodeposited Ni layer or polished bulk Ni surface, respectively, prior to the bead-blasting process. In addition to these two types of roughened, bead-blasted Ni surfaces, pristine samples of the electrodeposited Ni and polished Ni were also examined for their performance towards the OER. These four types of textured electrodes were characterized by SEM to confirm the general surface morphology of each type of electrode (Figure 1). The impact of the ~800-µm diameter glass particles during the bead-blasting process reshaped and increased both the surface area and roughness for the BB-edep and BB-pol surfaces. High magnification SEM images of the BB-edep, BB-pol, polished, and electrodeposited Ni electrodes are provided in the Supporting Information (SI). The bead-blasting process created irregular surfaces with a significant portion of these features exhibiting sharp peaks and valleys (Figures 1a and 1b). The electrodeposited and polished Ni substrates contained either textured surfaces with a nanoscale roughness or relatively smooth surfaces, respectively. The electrodeposited Ni coatings had a root mean square (RMS) roughness of 52 ± 8 nm (Figure 1c). The uniformity of the electrodeposited texture was largely dependent on the flux of $Ni^{2+}$ reactants to the electrode surfaces, as well as the surfactants in solution. Stirring of the bath at 250 rpm helped to improve the uniformity of the Ni layer through a consistent flux of $Ni^{2+}$, as well as the removal of hydrogen bubbles produced during the electrodeposition process.[37] The average grain

size of the electrodeposited Ni was ~150 nm. This smaller average grain size resulted in a relatively higher density of grains per unit area. In contrast, the polished cross-sections contained microscale crystalline grains (Figure 1d). The average diameter of the polished grains were ~8 μm. These differences in the grain size of the Ni within each type of electrode, as well as the methods used to prepare the electrodes (i.e., bead-blasting, electrodeposition, and polishing) created a series of samples each with a distinct surface roughness and $SA_f$.

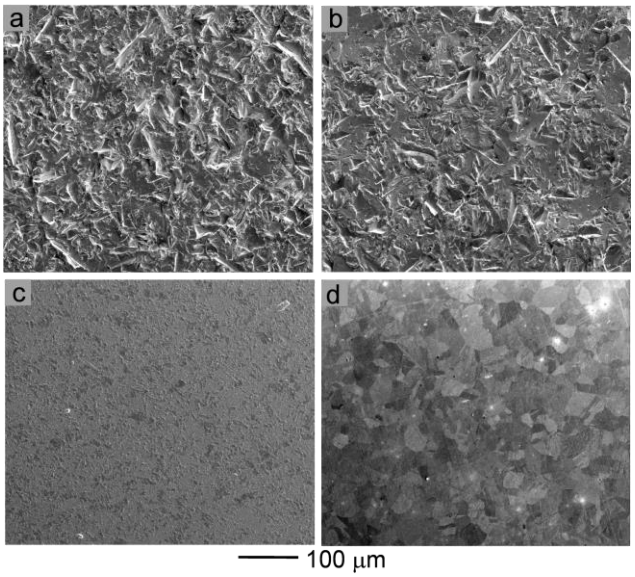


**Figure 1.** Representative scanning electron microscopy (SEM) images for: (a) electrodeposited Ni after bead-blasting (BB-edep); (b) polished Ni after bead-blasting (BB-pol); (c) planar electrodeposited Ni; and (d) planar polished Ni.

The morphology and surface areas of each type of textured electrode was further quantified using a 3D reconstruction of their surfaces based on a series of SEM analyses. Eucentric tilts of the samples were used to acquire SEM images at angles of 0 º and 15º. MountainsMap® software was used to process these stereoscopic images, resulting in the creation of 3D models. An example

of a 3D reconstructed view of these electrodes is provided in Figure S4 of the SI. From these 3D models, the relative $R_f$ were calculated for each type of Ni electrode. The $R_f$ values were calculated by dividing the 3D surface area by the geometric surface area ($A_{geo}$). Three independent replicates were prepared and separately evaluated for each type of Ni electrode. In addition, three measurements of the $R_f$ were obtained from random locations on each of the replicate electrodes to achieve an average of nine measurements for each type of electrode. The average values for the $R_f$ are reported in Table 1. For example, a $R_f$ of $1.3 \pm 0.2$ was calculated for both the BB-edep and BB-pol, which corresponds to a ~30% increase in $R_f$ when compared to the values for the polished Ni electrode. These measurements also indicated that each of the bead-blasted electrodes had similar values in terms of both the average $R_f$ and the spread in the measured values. Higher errors from the mean $R_f$ values were expected for the bead-blasted surfaces since these morphologies have a greater surface roughness relative to both the planar electrodeposited and polished surfaces. The average $R_f$ for the bead-blasted electrodes are also likely to be an underestimation of the actual increase in surface area due to limitations in the electron microscopy measurements. These limitations can result from sample charging, the effects of shadowing, and the influences of inherent magnetic fields within the sample. Further limitations to assessing the $R_f$ include the use of a 5-point moving average, which was used when creating the 3D models of these roughened surfaces. A key factor that contributes to an underestimation of the $R_f$ is the inability of the primary electron beam to visualize the buried or otherwise hidden surface areas on the bead-blasted Ni electrodes.

**Table 1.** Characteristics of the Textured Ni Electrodes.

| electrode type* | mean †$R_f$ | steady-state aging, avg *j* ($mA/cm^2$) ‡ | limited aging, avg *j* ($mA/cm^2$) ‡ |
|---|---|---|---|
| BB-edep | 1.3 ± 0.2 | 89.8 | 28.6 |
| BB-pol | 1.3 ± 0.2 | 82.3 | 32.8 |
| edep | 1.08 ± 0.02 | 68.1 | 33.4 |
| pol | 1.0 ± 0.01 | 60.7 | 53.2 |

* Abbreviations: BB = bead-blasted Ni; edep = electrodeposited Ni; pol = polished Ni.

† Local surface roughness factor ($R_f$) represents the reconstructed 3D surface area divided by the geometric surface area as determined through 3D reconstruction of SEM analyses using MountainsMap® software. The reported errors represent one standard deviation from the calculated mean values.

‡ Average current densities, *j*, as obtained from the linear sweep voltammetry plots at 1.1 V (vs Hg/HgO) under rotation at 7000 rpm.

The buried surface features within the bead-blasted electrodes were assessed by preparing cross-sections using FIB milling techniques. Analyses of these cross-sections by SEM confirmed the presence of cracks and buried voids within the outer most layers to a depth of ~5 μm for both types of bead-blasted samples. In general, surfaces with a smaller average grain size often have a greater material strength when compared to those with larger average grain sizes according to the Hall-Petch theory.[38, 39] Materials with a smaller grain size should also result in less deformation of their surfaces as a result of the bead-blasting process since there are a higher number of grain boundaries per unit area. For example, the dislocation of smaller grains during the bead-blasting process may be more inhibited since the direction of motion must change more frequently with a higher density of grain boundaries.[39, 40] Thus, less plasticity during bead-blasting was anticipated for the electrodeposited sample due to its smaller grain sizes when compared to the polished Ni. This phenomenon was, however, not observed in the cross-sections prepared by FIB milling. There were slightly more cracks and buried voids observed in the cross-sections of the BB-edep samples

than in the BB-pol samples. A representative cross-section obtained by FIB milling for the BB-edep sample is shown in Figure 2. Additional images of cross-sections prepared by FIB techniques can be found in Figures S5 and S6 in the SI. The higher degree of deformations in the BB-edep samples may have resulted from differences in the plasticity between the electrodeposited Ni grains and the underlying polished Ni substrate. The presence of cracks and buried voids in both the BB-edep and BB-pol samples indicates that there is an additional $SA_f$ that is not accounted for in these samples relative to the pristine electrodeposited and polished Ni. Consequently, the calculated $R_f$ underestimate the $SA_f$ for the bead-blasted electrodes.

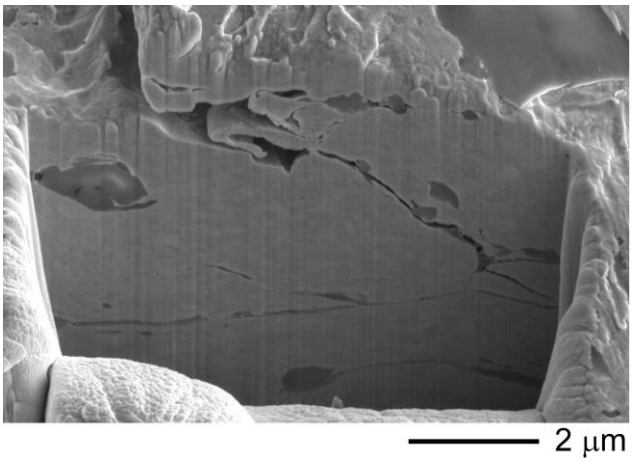


**Figure 2.** Representative SEM image of a cross-section prepared by focused ion beam (FIB) milling of the electrodeposited Ni electrode that was treated by bead-blasting. Secondary electrons were detected at a 52$^o$ tilt using an Everhart-Thornley detector.

*3.2 Elemental Analysis of the Ni Electrodes by Auger Electron Spectroscopy*

The elemental composition of the BB-edep and BB-pol was investigated by AES to determine whether trace impurities were incorporated into the electrodes as a result of the bead-blasting process. The presence of trace impurities, especially from other first row transition metals,

can influence the electrochemical activity of the OER.[41] For example, the inclusion of Fe into thin films of Ni oxide has been observed to influence the electrochemical performance of the OER, and can result in shifts to the peak potentials associated with the oxidative and reductive transformation of the β-$Ni(OH)_2$/β-NiOOH species.[42, 43] The silica particles used in the bead-blasting could be a source of contamination. Furthermore, any silica particles embedded in the surfaces of the Ni electrodes could block active surface area. Surface composition was analyzed by AES since it has a lower detection limit (~0.1 atomic %) for first row transition metals relative to XPS techniques.[44] The energy range chosen for the AES analyses (i.e., 480 to 900 eV) was established to include the LMM regions of Ni and several other first row transition metals, such as Fe, Mn, and Co.[45] Each of the nine Ni LMM transitions were identified in the region from 650 to 900 eV for the BB-edep and BB-pol electrodes. Five separate locations from each sample were analyzed by high resolution AES. No other first row transition metals were detected in the samples. Our analyses did not identify the presence of trace impurities within the detection limits of AES. These results suggest that impurities are not present in the surfaces, or that potential impurities are present below the detection limits of this surface sensitive technique. The results of our electrochemical measurements were attributed to the differences observed in the surface textures of the electrodes, as well as the inherent electrocatalytic activity of high purity Ni under the tested conditions, and the extent of the electrochemical aging.

Characterization of the Ni surface oxides and hydroxides was conducted using high resolution XPS analyses. Pristine samples of the electrodeposited and polished Ni exhibited a main emission peak at 852.6 eV, which indicates the presence of $Ni^0$ for the Ni $2p_{3/2}$ region (Figure S9 in the SI).[46] The polished Ni surface resembles more Ni oxide character when compared to the electrodeposited surface. The spectrum for the electrodeposited surface has a character that is more

similar to that of Ni metal, which was expected since these deposits were formed under reducing potentials. In contrast, the Ni rod was prepared by cold extrusion methods. Satellite peaks that result from multiplet splitting, shake-up, and plasmon loss structures can cause difficulty in the interpretation of the Ni 2p region. Previous work on the quantitative assignment of Ni oxide, hydroxide, and (oxy)hydroxide peaks have used the Gupta and Sen multiplet fitting envelopes.[46] These fitting envelopes account for variations in the binding energies associated with these satellite peaks. Since the β-NiOOH phase is formed under an applied potential during electrochemical aging, we expected that the electrode surface would relax from the β-NiOOH phase to the β-$Ni(OH)_2$ phase after removal from the electrochemical set-up. As an indirect assessment of the β-NiOOH phase, the uniformity of the β-$Ni(OH)_2$ phase was inspected directly after steady-state electrochemical aging for the BB-pol sample. The XPS data for the aged BB-pol sample exhibits a main emission peak at 854.6 eV. This binding energy is assigned to a $Ni^{2+}$ oxidation state.[6, 46, 47] The absence of a Ni $2p_{3/2}$ peak at the lower binding energies indicates that the hydroxide surface phase is uniform over the analyzed area (700 μm x 400 μm) and to the mean escape depth of the detected photoelectrons (~10 nm).

*3.3 Electrochemical Aging by Cyclic Voltammetry Techniques*

Electrochemical aging of Ni-based electrodes between the Ni (II) and Ni (III) redox states can enhance their performance towards the OER.[7, 14, 48, 49] The growth of the anodic and cathodic peaks with consecutive CV scanning demonstrate an increase in the amount of β-NiOOH on the Ni surfaces and consequently an improvement in their activity.[16] The potential range of 0 to 0.6 V (vs Hg/HgO) was selected to exclude Faradaic current from the OER during the processes associated with the electrochemical aging. More pronounced structural deformations on the

surfaces of Ni-based electrodes can occur when the electrochemical aging process includes more oxidizing potentials.[14, 15, 24] Minimal structural changes were observed for the electrochemically aged electrodes as indicated by the SEM measurements (Figure S10 in the SI). A relatively fast scan rate (i.e., 100 mV/s) was selected for the electrochemical aging since the high repetition of the potential scanning by CV was essential to attain the improved OER performance. The use of a slower CV scan rate was found to be ineffective at obtaining a steady-state response within a reasonable period (e.g., less than 48 h) during the electrochemical aging. Two types of electrochemical aging, a steady-state and a limited aging process, were evaluated for their influence on the OER as a function of the distinct micro- and nanoscale textures of the Ni electrodes.

*3.4 Steady-State Electrochemical Aging*

To achieve a high electrocatalytic activity for the OER, it is desired that the β-NiOOH phase form a continuous layer over the surfaces of the Ni electrodes. This process of achieving a stable, electrochemically derived active state for each sample was referred to as the "steady-state aging" process. The samples were determined to have achieved the desired behavior when the anodic peaks at ~0.42 and ~0.48 V (vs Hg/HgO) exhibited minimal changes between at least ten consecutive CV scans for the planar and bead-blasted electrodes, respectively. Specifically, when this peak stabilized within ± 10 μA and did not exhibit further shifts in the peak potential (e.g., ± 1 mV) with successive CV scans, it was assumed that the electrode was in a pseudo-stable steady-state. These conditions implied that the amount of β-NiOOH present on the surfaces of the electrodes was no longer changing with further electrochemical treatment. The voltammograms from the steady-state aging process for the bead-blasted electrodes exhibited sharp anodic peaks

with higher peak current densities (Figures 3a and 3c) relative to the electrodeposited or polished Ni electrodes (Figures 3e and 3g). From these results, it can be inferred that after this aging process there is a larger amount of β-NiOOH per $A_{geo}$ on the bead-blasted samples relative to the planar Ni electrodes. This assessment is consistent with the increase in electrode surface area that resulted from the bead-blasting process. The planar electrodes of electrodeposited and polished Ni each required ~70 and ~80 CV scans, respectively, to achieve a steady-state electrochemical response. In contrast, the bead-blasted electrodes required ~100 times more CV scans to achieve the same response. Diffusion of electrolyte to all of the surfaces on the bead-blasted electrodes was likely hindered by their buried nature, which slowed down the electrochemical transformation. This large difference in the number of CV scans required to reach a stable response was likely due to the limited mass transfer of fresh electrolyte into the recesses of the highly textured bead-blasted surfaces. It is hypothesized that the number of CV scans required for each of the Ni electrodes to reach a steady-state was largely dependent on the accessibility of electrolyte to all of the $SA_f$. The electrolyte must adequately reach all of the surfaces for transformation to the electrochemically active β-NiOOH phase.

Shifts in the anodic peak potentials were observed in the CV profiles obtained during the steady-state electrochemical aging for the BB-edep and BB-pol electrodes. Anodic peak potentials for the bead-blasted electrodes were initially centered at 0.45 V (vs Hg/HgO). After steady-state electrochemical aging, the anodic peak potentials shifted to 0.48 V (vs Hg/HgO) (Figures 3a and 3c). Similar shifts in the anodic peak potentials have been previously reported for Ni electrodes aged by either immersion in alkaline electrolyte or by potential cycling across the Ni (II/III) redox peak.[7, 16, 36, 50] This shift of the anodic peak to higher potentials has been attributed to the structural transformation of β-$Ni(OH)_2$ to the β-NiOOH phase as observed by *in situ* Raman spectroscopy

studies of electrodes previously aged in Fe-free 1 M KOH.[36] An increase in the amount of the β-$Ni(OH)_2$ and β-NiOOH present on the surfaces of an electrode will likely decrease the rate of electrolyte mass transfer to the reactive interface. A greater impedance associated with this electrochemical transformation will result if the newly formed (oxy)hydroxide phases extend beneath the outermost surface layers. These impedance effects are likely the cause of the observed peak shift (i.e., 0.03 V) for the bead-blasted electrodes. The anodic peak potentials for the planar samples of electrodeposited and polished Ni remained at ~0.42 V (vs Hg/HgO) as exhibited in Figures 3e and 3g. The absence of an anodic peak shift for these samples was likely due to the relatively few CV scans required to reach a steady-state condition. The prolonged electrochemical treatment required by the bead-blasted surfaces was, as mentioned above, likely due to the increased and buried $SA_f$ of these electrodes. The flux of electrolyte to and from these surfaces was aided by rotating the electrodes during the aging process. This increased flux improved the rate at which the electrode surfaces became electrochemically "aged" since this process requires a reaction with the dissolved species in the electrolyte solution. Although a relatively high speed of rotation (i.e., 5500 rpm) was utilized in these experiments, it is likely that not all of the buried surfaces within the roughened, bead-blasted textures received fresh electrolyte or a consistent flux during consecutive scanning by CV.

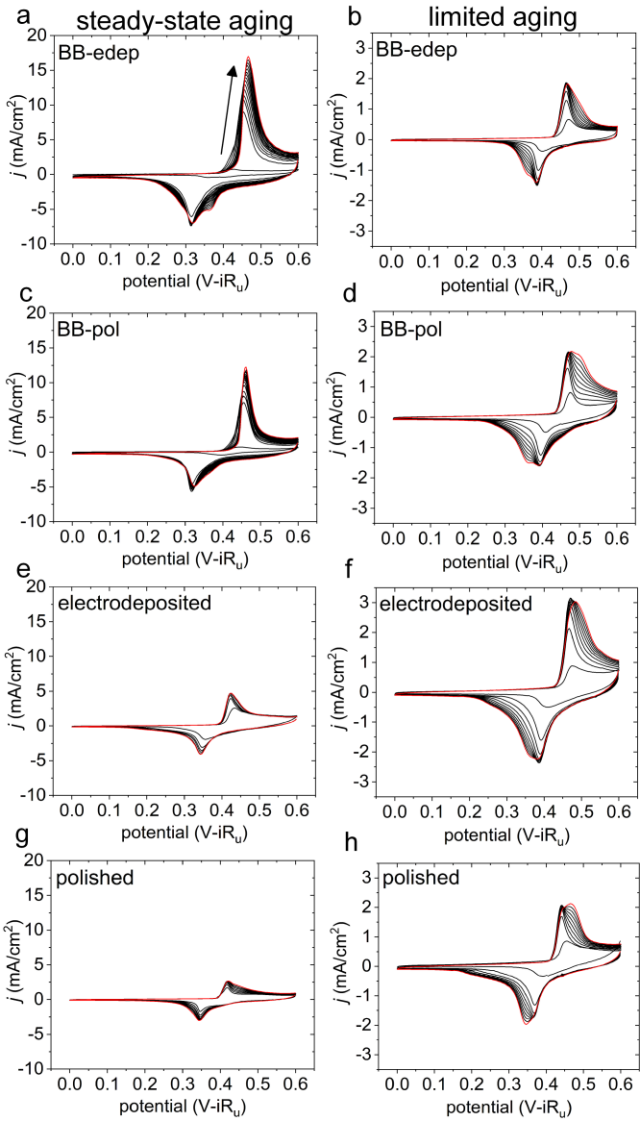


**Figure 3.** Representative trends for the electrochemical aging of the textured Ni electrodes by cyclic voltammetry (CV). The arrow in (a) indicates the trend of the progressive CV profiles. The data in the left column is from the steady-state aging sequence, showing every 500$^{th}$ CV scan in (a, c) and every 10$^{th}$ CV scan in (e, g). The right column contains data from the limited aging sequence, showing every 10$^{th}$ CV scan in (b, d, f, and h). The last CV scan for each sequence is indicated by the profiles highlighted in red. The sequences correspond to (a, b) the BB-edep electrode, (c, d) the BB-pol electrode, (e, f) the planar Ni electrode with an electrodeposited finish, and (g, h) the planar Ni electrode with a polished finish. All data was normalized to the theoretical

surface area ($SA_f$). The CV scans were acquired at a scan rate of 100 mV/s in purified 1 M KOH. Each electrode was rotated at 5500 rpm for the duration of each sequence of measurements.

*3.5 Limited Electrochemical Aging*

The textured electrodes were also evaluated using a second type of electrochemical aging technique. This type of treatment was referred to as the "limited aging" process. In this process, each electrode was aged with a set number of CV scans prior to assessing its performance towards the OER. The limited aging process conducted 100 sequential CV scans regardless of whether or not each electrode had reached a steady-state electrochemical response. As anticipated, a steady-state response was not achieved for the bead-blasted electrodes (Figures 3b and 3d). Conversely, the planar electrodes of electrodeposited or polished Ni were able to reach a steady-state condition during the limited aging process (Figures 3f and 3h), but continued CV scanning was performed beyond this response. For example, the electrodeposited Ni achieved a stable intensity in their CV profile after the 42$^{nd}$ CV scan as observed by its consistent anodic peak. A similar behavior was observed for the polished Ni electrode, which reached a stable electrochemical behavior at the 40$^{th}$ CV scan. After 10 to 15 CV scans beyond the stable state, the anodic peak broadened, which likely indicated a further conversion of β-$Ni(OH)_2$ to β-NiOOH beneath the outermost surfaces of these electrodes. Subtle shifts in peak position and distortions to the peak shape can also result from variations in the pH at the electrode surfaces.[50] The underlying principles of Nernstian thermodynamics describe the relationship between the concentrations of Faradaic species, rates of the reaction, and the observed potentials for electrochemical reactions.[51] Increasing the pH of an electrolyte can increase the magnitude of the redox wave for the transformation of Ni (II) to Ni (III).[52] Since the electrolyte composition and concentration were consistent for all of our

experiments, large variations in pH should not play a dominant role in the observed differences of the redox properties for the textured surfaces. The limited aging process was applied to each type of electrode to assess whether a less uniform coverage of β-NiOOH on the bead-blasted electrodes would influence their relative performance towards the OER. In general, the current densities calculated for the anodic and cathodic peaks following the limited aging process (~2 to 3 $mA/cm^2$) were relatively similar for all four types of Ni electrodes. Since the anodic and cathodic peaks were similar in their current densities, it can be inferred that comparable amounts of β-NiOOH were present on the surfaces of the electrodes but with varying degrees of coverage.

*3.6 Assessment of Performance towards the Oxygen Evolution Reaction*

Directly after performing either the steady-state or the limited aging treatment, the electrodes were assessed for their OER activity. This assessment was conducted through LSV measurements acquired at relatively slow scan rates (i.e., 1 mV/s). All current densities shown in the LSV plots were normalized against the theoretical $SA_f$ for each type of electrode as determined from the 3D models of their textured surfaces. Figure 4 contains the LSV responses for each type of electrode, which were obtained at both a slow and fast rotational speed (i.e., 1000 and 7000 rpm). The current density response as a function of applied potential exhibited a consistent trend between the different types of electrodes regardless of the rotational speed. Additional LSV responses for the electrochemically aged electrodes at other rotational speeds are provided in the SI. These analyses enable a direct comparison of the effects of both electrochemical aging and the texture of the electrodes.

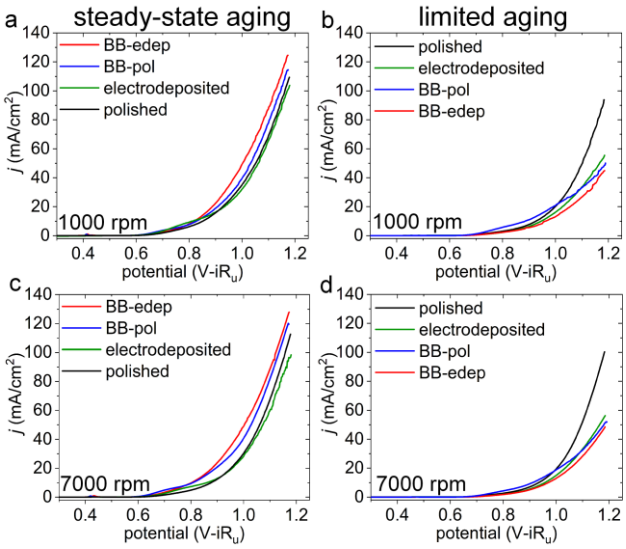


**Figure 4.** Representative linear sweep voltammetry (LSV) plots acquired at 1 mV/s in 1 M KOH. All data has been normalized to the theoretical $SA_f$. Prior to acquiring these LSV plots the electrodes were treated by either (a, c) the steady-state aging process or (b, d) the limited aging process. The plots in (a) and (b) were acquired while rotating the Ni working electrodes at 1000 rpm, while the plots in (c) and (d) were acquired at a rotational speed of 7000 rpm.

The steady-state aging process created electrodes that exhibited lower onset potentials for the OER relative to the samples processed by the limited aging treatment. The reaction onset potential, also referred to as the overpotential, is a measure of the increase in the applied potential needed to drive a reaction beyond the value predicted by purely thermodynamic conditions. This onset potential is dependent on the electrochemical conditions (e.g., concentration and temperature of the electrolyte) and the type of electrocatalyst used in the reaction (e.g., its elemental composition).[53] Similar onset potentials to the OER were observed for all electrodes treated by the same type of aging technique. The steady-state aging treatment decreased the overpotentials by ~55 mV (Figures 4a and 4c). A similar reduction in overpotentials has been observed for other electrochemically aged Ni electrodes.[7] Previous work has calculated turnover frequencies for

electrochemically aged Ni to be 23 times higher than for non-aged Ni.[7] Godwin *et al*. concluded that the electrochemically aged Ni electrodes were more active due to the transformation of the Ni surfaces into the more active β-phase.[7] Differences in the performance of the electrodes are, in general, inherent to their surface morphology and $SA_f$, as well as to the type of aging process used to condition the electrodes.

The bead-blasted electrodes exhibited a better electrochemical performance after the steady-state aging process than the planar samples of polished or electrodeposited Ni as observed in the LSV measurements. The trends in the LSV measurements of the electrodes treated by steady-state aging can be correlated to the relative amount of the active β-NiOOH phase present on the surfaces of each type of electrode. The $SA_f$ gained from the bead-blasting process is observed in the relatively high current densities achieved by these samples. The BB-edep electrode achieved the highest current densities of all the samples at potentials beyond 0.9 V (vs Hg/HgO) in the LSV plots (Figures 4a and 4c). After the steady-state aging process, the CV scan of the BB-edep electrode also showed the highest anodic peak area. The nanoscale grains at the surfaces of the BB-edep electrodes may enable an increased diffusion of electrolyte into the buried voids near the outermost surfaces of these electrodes (Figure 2). The smaller grains of the BB-edep samples relative to the larger grains of the BB-pol samples could also impact the accessible $SA_f$ following the steady-state aging process. It is possible that hydrophilic channels form within the cracks around the Ni grains after their surfaces are covered with β-NiOOH as a result of the steady-state aging process. The higher number of grain boundaries in the electrodeposited Ni may have enabled the diffusion of more electrolyte into the buried voids of these bead-blasted materials during the steady-state aging process. In summary, it is likely that an increase in $SA_f$ was associated with the

improved performance observed for the electrodeposited bead-blasted samples towards the OER as shown in Figure 4.

The limited aging process resulted in the polished Ni electrodes exhibiting the highest current densities at potentials beyond 1.0 V (vs Hg/HgO). The smooth, planar surfaces of the polished Ni electrodes prevented oxygen bubbles from being trapped on their surfaces, especially when subjected to a high shear flow. The flow of the electrolyte may not uniformly access all of the $SA_f$ for the other, more textured samples. The flux of electrolyte near the electrode was the same for all of the samples, but the efficiency of mass transfer processes to and from all of the Ni surfaces was likely different for each type of electrode. The polished Ni electrode experienced the highest mass transfer efficiency and, thus, demonstrated much higher current densities for the OER at high overpotentials (Figures 4b and 4d). The enhanced performance towards the OER for the polished Ni was likely not due to a larger amount of β-NiOOH on their surfaces since the CVs from the limited aging treatment did not show substantially greater anodic and cathodic peak areas relative to the other samples. Their enhanced OER performance was more likely due to the lack of roughness on the surfaces of these electrodes. Interestingly, the planar electrodes of electrodeposited Ni had a lower overall performance in comparison to the polished Ni although these electrodes had a similar $R_f$.

The lower efficiency of the electrodeposited Ni relative to the polished Ni after treatment by the limited aging process may likely be a consequence of the nanoscale roughness. This nanoscale variation in surface roughness may disrupt the shear flow of electrolyte across their surfaces. It is possible that nanoscale bubbles may become pinned to multiple grains on the surfaces of the electrodeposited Ni, which would block its $SA_f$ and contribute to a reduction in its OER performance. The planar electrodeposited Ni performed only slightly better than the bead-

blasted textures (i.e., BB-edep or BB-pol) at applied potentials greater than 1.0 V (vs Hg/HgO) (Figure 4b and 4d). Furthermore, since the limited aging technique allowed CV scanning to continue beyond the steady-state (i.e., beyond the 42$^{nd}$ CV scan), it may be possible that there are disparities in the type or thickness of active Ni phases present on the electrode surfaces that could otherwise impact their electrochemical performance.[54] For example, performing CV scanning beyond the steady-state response typically resulted in broadening and a shift to a higher anodic peak potential. This peak broadening and shift in peak potential may indicate a more resistive condition caused by slower rates of mass transfer that result from a thicker and possibly more disordered β-NiOOH phase. Non-uniform aging of the nanoscale grains in the electrodeposited Ni may also contribute to their lower current densities than observed for the polished Ni. The bead-blasted electrodes also experienced a non-uniform, inadequate aging by the limited treatment.

The irregular textures of the bead-blasted electrodes prevented electrolyte from efficiently reaching all of the surfaces. The limited aging treatment likely resulted in a non-uniform surface coverage of the β-NiOOH phase. At potentials greater than 1.0 V (vs Hg/HgO), both the BB-edep and BB-pol electrodes exhibited a lower relative performance when treated by this process. This reduced performance could be a result of oxygen bubbles adhering to the recessed surfaces of the bead-blasted electrodes, resulting in an ineffective mass transfer. The $SA_f$ gained from the bead-blasting process is underutilized for samples treated by the limited aging process. The LSV measurements acquired after steady-state aging indicated a better utilization of the increased $SA_f$ gained from the bead-blasting process.

The electrochemical performance of each of the textured Ni electrodes towards the OER was further evaluated by CP measurements obtained at 500 mA/cm$^2$ over a period of 7 min. The duration of this experiment was sufficient stabilization of the current response of each type of

electrode (Figure 5). Commercial water electrolyzers require electrocatalysts that can sustain current densities at or above 500 mA/cm$^2$.[21, 54] Hence, an industrially relevant current density of 500 mA/cm$^2$ with respect to the geometric area was chosen to probe the OER activity in these CP measurements. In general, differences in the current densities between the samples were most apparent when rotated at lower rotational speeds. At the lower rotational speeds, the samples were more hindered by mass transfer, and the influence of electrode morphology was more apparent. Periodic oscillations in the data indicate the release of oxygen bubbles from the electrodes.[24, 25] The electrodes treated by steady-state aging exhibited lower potentials in the CP measurements and a smaller amplitude in the oscillations of these potentials over time.

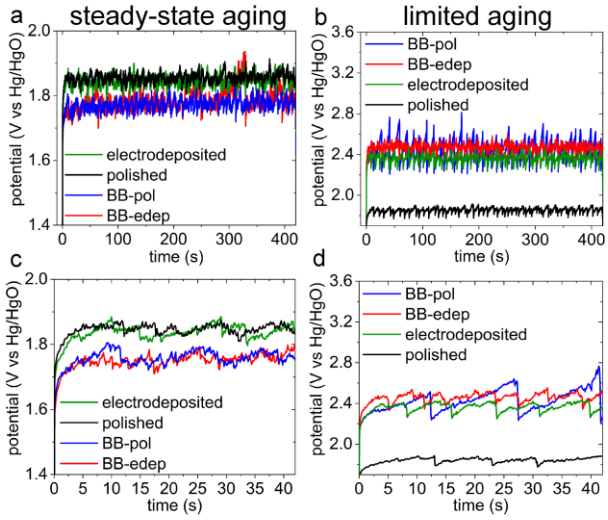


**Figure 5.** Representative chronopotentiometry (CP) plots acquired at 500 mA/cm$^2$ in 1 M KOH while rotating each electrode at 500 rpm. Prior to the CP measurements, the electrodes in (a, c) were aged by the steady-state aging process, while the electrodes in (b, d) were treated by a limited aging process. The plots in (c, d) show shorter time-scales corresponding to the data plotted in (a, b).

During the OER, a higher efficiency for the generation and release of bubbles was observed for the electrodes treated by the steady-state aging process. In the CP experiments, these samples exhibited lower potentials on average at 500 mA/cm$^2$, as well as a higher frequency and smaller amplitude in the oscillations of these potentials (Figures 5a and 5c). These results indicated that the steady-state aged samples demonstrated higher rates for both the production and release of bubbles. All of the electrodes aged by the steady-state process exhibited a similar character in terms of the amplitude of their oscillations during the CP measurements. This similarity in the data indicates that these samples had a comparable behavior towards bubble release regardless of their nanoscale and/or microscale textured surfaces. The BB-edep and BB-pol samples did, however, achieve a lower average potential at 500 mA/cm$^2$ relative to the planar electrodes. These trends in performance remained consistent even at higher rotational speeds. In addition, the applied current density of 500 mA/cm$^2$ was calculated for each sample based on their $A_{geo}$, which resulted in a lower current density in practice for the BB-edep and BB-pol samples relative to the planar electrodes after accounting for their estimated $SA_f$. For the tested conditions, the bead-blasted electrodes exhibited a slightly better performance, operating at ~0.2 V lower than the planar electrodes. It is anticipated that a further improvement in performance would have been observed for the bead-blasted electrodes if the additional $SA_f$ had been accounted for in the CP measurements. The samples aged by steady-state techniques also approached the commercially relevant potential of ~1.6 V (vs Hg/HgO) at 500 mA/cm$^2$.[21] It has been proposed that these targeted operating conditions are necessary to meet the requirements of commercial electrolyzers.[21, 55] From the results of the CP measurements, it can be concluded that steady-state aging is the more favorable method for conditioning electrodes with a relatively high $SA_f$, such as the microscale textures of the bead-blasted electrodes.

For the electrodes treated by the limited aging technique, the polished Ni electrodes exhibited the most stable electrochemical response and the lowest potentials in their CP plots. The results in Figures 5b and 5d indicated that the polished electrodes had less surface passivation with oxygen bubbles while operated at 500 mA/cm$^2$. The electrochemical response of the polished Ni electrode also stabilized at the lowest potential at ~1.8 V (vs Hg/HgO), while the other samples stabilized at ~2.4 V (vs Hg/HgO). For these limited aging conditions, as stated above, the polished Ni electrodes were able to remove oxygen bubbles most efficiently at all of the rotational speeds due to their relatively smooth morphology.

In addition to electrochemical aging of electrodes, the orientation of the electrode is also a factor that can influence the accumulation of gas bubbles and, thus, an electrode's activity for the OER. To evaluate the performance of the textured electrodes in alternative orientations, the Ni electrodes were held without rotation in a face-up configuration. The samples were each treated by the steady-state aging technique. This experimental configuration decreased the flux of electrolyte to the electrode surfaces. Each of these samples stabilized at higher potentials in the CP measurements than under conditions of an induced shear flow (Figure S23 in the SI). This change was attributed to the reduced rates of electrolyte flux and other components of mass transfer. Under these conditions, both types of bead-blasted Ni electrodes exhibited an improved performance towards the OER in comparison to the planar samples of polished Ni or electrodeposited Ni. For example, the bead-blasted electrodes had a higher number of bubble release events per unit time. The microscale texture and the high $SA_f$ of the bead-blasted electrodes were beneficial for the growth and release of gas bubbles. Microscale recessed features have been previously observed to exhibit enhanced efficiencies for the OER at high potentials.[24, 25] This enhancement has been attributed to their ability to promote the generation of relatively small bubbles and to exhibit a

higher frequency of bubble release events as indicated by the electrochemical measurements. Furthermore, the presence of nanoscale textures on the surfaces of microscale features may add an additional enhancement to the mass transfer abilities of a textured electrode.[55]

The results from this study highlight the importance of electrochemical aging of Ni electrodes for assessing their OER activity, especially for electrodes with textured surfaces. The electrochemical aging of Ni electrodes may also better mimic their performance under industrial conditions since a more thermodynamically stable state is achieved under these conditions. When electrodes are sufficiently aged, their characteristics for electrolyte wetting and gas bubble formation likely improve due to a more uniform coating of the β-NiOOH phase on their surfaces.[56] Bead-blasting of Ni electrodes produced a microscale texture that, when aged to a steady-state condition, had a higher activity towards the OER than electrodes with a relatively smooth texture. These sufficiently aged electrodes exhibited higher current densities (i.e., a gain of 50 $mA/cm^2$ at 1.1 V vs Hg/HgO) when compared to electrodes treated by a limited aging method. The CP data indicated a reduction of 0.7 V in the potential required for the OER at an applied current density of 500 $mA/cm^2$ for the electrodes aged by steady-state conditions. In addition, the bead-blasted electrodes demonstrated a slightly lower potential response (a decrease of ~ 0.2 V) at 500 $mA/cm^2$ relative to the planar electrodes of electrodeposited Ni or polished Ni after aging each electrode by the steady-state method. These improvements may be a result of the microscale texture, which may favor the production of smaller diameter bubbles and a more frequent release of bubbles from their surfaces. Furthermore, the presence of nanoscale grains on the surfaces of the BB-edep electrodes may enable an improved mass transfer (e.g., diffusion and migration) of reactants and products due to a higher number of hydrophilic channels formed at grain boundaries within the electrodeposited layer. Additional $SA_f$, which was not detected during the SEM-based analyses,

may also contribute to the observed improvements in performance for the bead-blasted samples. Bead-blasting increased the $SA_f$ by ≥30% at a relatively fast rate (~ 6 $cm^2$/min) and could be applied to large electrodes used in electrocatalytic systems. New electrode surface textures could be prepared by further refinement of the bead-blasting parameters (e.g., tuning the composition of the particles, acceleration of these particles, and average particle diameter).

## 4. CONCLUSIONS

Microscale surface textures on Ni electrodes were prepared by a simple, scalable bead-blasting method. These roughened surface morphologies were assessed for their performance towards the OER after performing two distinct types of electrochemical aging. One type of electrochemical aging utilized consecutive CV scanning until achieving a "steady-state" for the conversion of the Ni surfaces to a β-NiOOH phase. The other type of electrochemical aging was a "limited aging" process where only 100 consecutive CV scans were performed regardless of the anodic peak stability. In addition to performing either type of electrochemical aging, the composition and texture of each electrode were carefully controlled to establish links between their performance for the OER and their surface morphology. Three-dimensional models of the textured surfaces based on SEM analyses were used to estimate the $R_f$ values and resulting $SA_f$ for each type of textured electrode. These estimations of the $SA_f$ were used to calculate the apparent current densities for the electrochemical LSV measurements. The estimated $SA_f$ for each type of texture aided in correlating their OER performance to their surface morphology. The bead-blasted Ni electrodes outperformed the planar Ni electrodes with either a polished finish or a nanoscale texture when each of these electrodes were sufficiently aged through a steady-state aging process. For example, in the CP measurements the bead-blasted electrodes stabilized at 0.2 V below the other types of electrodes at an applied current density of 500 $mA/cm^2$. In contrast, when a limited aging method was used the relatively smooth and featureless morphologies (i.e., polished Ni) had the highest performance for the OER as observed in both the CP and LSV measurements. These results emphasize the importance of assessing the performance of textured electrodes towards the OER after sufficiently aging the samples. Highly textured surfaces will likely require prolonged aging and can also be hindered by the presence of trapped bubbles in their recessed features.

Further studies are warranted to further tune the bead-blasting techniques for creating textured electrodes. For example, this process could use smaller diameter particles to enable a scalable approach to preparing nanoscale textures.

## ASSOCIATED CONTENT

*Supporting Information*

The Supporting Information for this article is available via the internet free of charge.

Additional SEM images, CV profiles, results from the LSV, CP, and CA measurements, XPS data, table of cathodic charges, literature review on the effects of electrochemical aging, and results from the AES analyses

## ACKNOWLEDGEMENTS

This research was supported in part by the Natural Sciences and Engineering Research Council (NSERC) of Canada (Discovery Grant No. 1077758), the Canada Research Chairs Program (B.D. Gates, Grant No. 950-215846), the Engineered Nickel Catalysts for Electrochemical Clean Energy project administered from Queen's University (Grant No. RGPNM 477963-2015) from the NSERC of Canada Discovery Frontiers Program, and CMC Microsystems (MNT Financial Assistance, Grant No. 5030). This work made use of the 4D LABS (www.4dlabs.ca) and the Center for Soft Materials shared facilities supported by the Canada Foundation for Innovation (CFI), British Columbia Knowledge Development Fund (BCKDF), Western Economic Diversification Canada, and Simon Fraser University.

## REFERENCES


(1) Dresp, S.; Luo, F.; Schmack, R.; Kühl, S.; Gliech, M.; Strasser, P. An Efficient Bifunctional Two-Component Catalyst for Oxygen Reduction and Oxygen Evolution in Reversible Fuel Cells, Electrolyzers and Rechargeable Air Electrodes. *Energy Environ. Sci.* **2016**, *9*, 2020–2024.

(2) Wang, Z. L.; Xu, D.; Xu, J. J.; Zhang, X. B. Oxygen Electrocatalysts in Metal-Air Batteries: From Aqueous to Nonaqueous Electrolytes. *Chem. Soc. Rev.* **2014**, *43*, 7746–7786.

(3) Suen, N.-T.; Hung, S.-F.; Quan, Q.; Zhang, N.; Xu, Y.-J.; Chen, H. M. Electrocatalysis for the Oxygen Evolution Reaction: Recent Development and Future Perspectives. *Chem. Soc. Rev.* **2017**, *46*, 337–365.

(4) Marini, S.; Salvi, P.; Nelli, P.; Pesenti, R.; Villa, M.; Berrettoni, M.; Zangari, G.; Kiros, Y. Advanced Alkaline Water Electrolysis. *Electrochim. Acta* **2012**, *82*, 384–391.

(5) Li, X.; Walsh, F. C.; Pletcher, D. Nickel Based Electrocatalysts for Oxygen Evolution in High Current Density, Alkaline Water Electrolysers. *Phys. Chem. Chem. Phys.* **2011**, *13*, 1162–1167.

(6) Hall, D. S.; Bock, C.; MacDougall, B. R. The Electrochemistry of Metallic Nickel: Oxides, Hydroxides, Hydrides and Alkaline Hydrogen Evolution. *J. Electrochem. Soc.* **2013**, *160*, F235–F243.

(7) Godwin, I. J.; Lyons, M. E. G. Enhanced Oxygen Evolution at Hydrous Nickel Oxide Electrodes via Electrochemical Ageing in Alkaline Solution. *Electrochem. Commun.*

**2013**, *32*, 39–42.

(8) Lyons, M. E. G.; Russell, L.; O'Brien, M.; Doyle, R. L.; Godwin, I.; Brandon, M. P. Redox Switching and Oxygen Evolution at Hydrous Oxyhydroxide Modified Nickel Electrodes in Aqueous Alkaline Solution: Effect of Hydrous Oxide Thickness and Base Concentration. *Int. J. Electrochem. Sci.* **2012**, *7*, 2710–2763.

(9) Lyons, M. E. G.; Doyle, R. L.; Godwin, I.; O'Brien, M.; Russell, L. Hydrous Nickel Oxide: Redox Switching and the Oxygen Evolution Reaction in Aqueous Alkaline Solution. *J. Electrochem. Soc.* **2012**, *159*, H932–H944.

(10) Hall, D. S.; Lockwood, D. J.; Bock, C.; MacDougall, B. R. Nickel Hydroxides and Related Materials: A Review of Their Structures, Synthesis and Properties. *Proc. R. Soc. A* **2015**, *471*, 20140792.

(11) Hall, D. S.; Lockwood, D. J.; Poirier, S.; Bock, C.; MacDougall, B. R. Applications of in Situ Raman Spectroscopy for Identifying Nickel Hydroxide Materials and Surface Layers during Chemical Aging. *ACS Appl. Mater. Interfaces* **2014**, *6*, 3141–3149.

(12) Oshchepkov, A. G.; Bonnefont, A.; Saveleva, V. A.; Papaefthimiou, V.; Zafeiratos, S.; Pronkin, S. N.; Parmon, V. N.; Savinova, E. R. Exploring the Influence of the Nickel Oxide Species on the Kinetics of Hydrogen Electrode Reactions in Alkaline Media. *Top. Catal.* **2016**, *59*, 1319–1331.

(13) Oshchepkov, A. G.; Bonnefont, A.; Parmon, V. N.; Savinova, E. R. On the Effect of Temperature and Surface Oxidation on the Kinetics of Hydrogen Electrode Reactions on Nickel in Alkaline Media. *Electrochim. Acta* **2018**, *269*, 111–118.

(14) Li, H.; Shao, Y.; Su, Y.; Gao, Y.; Wang, X. Vapor-Phase Atomic Layer Deposition of Nickel Sulfide and Its Application for Efficient Oxygen-Evolution Electrocatalysis. *Chem. Mater.* **2016**, *28*, 1155–1164.

(15) Shinagawa, T.; Ng, M. T. K.; Takanabe, K. Boosting the Performance of the Nickel Anode in the Oxygen Evolution Reaction by Simple Electrochemical Activation. *Angew. Chemie* **2017**, *129*, 5143–5147.

(16) Lyons, M. E. G.; Brandon, M. P. The Oxygen Evolution Reaction on Passive Oxide Covered Transition Metal Electrodes in Aqueous Alkaline Solution. Part 1-Nickel. *Int. J. Electrochem. Sci.* **2008**, *3*, 1386–1424.

(17) Alsabet, M.; Grde, M.; Jerkiewicz, G. Electrochemical Growth of Surface Oxides on Nickel. Part 3: Formation of β-NiOOH in Relation to the Polarization Potential, Polarization Time, and Temperature. *Electrocatalysis* **2015**, *6*, 60–71.

(18) Rinaldi, A. L.; Carballo, R. Impedimetric Non-Enzymatic Glucose Sensor Based on Nickel Hydroxide Thin Film onto Gold Electrode. *Sensors Actuators, B Chem.* **2016**, *228*, 43–52.

(19) Smith, R. D. L.; Sherbo, R. S.; Dettelbach, K. E.; Berlinguette, C. P. On How Experimental Conditions Affect the Electrochemical Response of Disordered Nickel Oxyhydroxide Films. *Chem. Mater.* **2016**, *28*, 5635–5642.

(20) Fan, C.; Piron, D. L. Electrodeposition as a Means of Producing Large-Surface Electrodes Required in Water Electrolysis. *Surf. Coatings Technol.* **1995**, *73*, 91–97.

(21) Zhou, H.; Yu, F.; Zhu, Q.; Sun, J.; Qin, F.; Yu, L.; Bao, J.; Yu, Y. Water Splitting by

Electrolysis at High Current Density under 1.6 Volts. *Energy Environ. Sci.* **2018**, 6, 3–5.

(22) Zeng, K.; Zhang, D. Evaluating the Effect of Surface Modifications on Ni Based Electrodes for Alkaline Water Electrolysis. *Fuel* **2014**, *116*, 692–698.

(23) Bae, S.; Kim, H.; Lee, Y.; Xu, X.; Park, J. S.; Zheng, Y.; Balakrishnan, J.; Lei, T.; Ri Kim, H.; Song, Y. I; Kim, Y. J. Roll-to-Roll Production of 30-Inch Graphene Films for Transparent Electrodes. *Nat. Nanotechnol.* **2010**, *5*, 574–578.

(24) Taylor, A. K.; Andreu, I.; Gates, B. D. Regular Dimpled Nickel Surfaces for Improved Efficiency of the Oxygen Evolution Reaction. *ACS Appl. Energy Mater.* **2018**, *1*, 1771–1782.

(25) Paul, M. T. Y.; Yee, B. B.; Bruce, D. R.; Gates, B. D. Hexagonal Arrays of Cylindrical Nickel Microstructures for Improved Oxygen Evolution Reaction. *ACS Appl. Mater. Interfaces* **2017**, *9*, 7036–7043.

(26) Ahn, S. H.; Hwang, S. J.; Yoo, S. J.; Choi, I.; Kim, H. J.; Jang, J. H.; Nam, S. W.; Lim, T. H.; Lim, T.; Kim, S. K.; Kim, J. J. Electrodeposited Ni Dendrites with High Activity and Durability for Hydrogen Evolution Reaction in Alkaline Water Electrolysis. *J. Mater. Chem.* **2012**, *22*, 15153–15159.

(27) Kuhn, A. T.; Bin Yusof, J.; Hogan, P. The Role of Electrode Structure and Surface Texture in the Performance of Gas Evolving Electrodes. *J. Appl. Electrochem.* **1979**, *9*, 765–775.

(28) Bocca, C.; Barbucci, A.; Cerisola, G. The Influence of Surface Finishing on the Electrocatalytic Properties of Nickel for the Oxygen Evolution Reaction (OER) in

Alkaline Solution. *Int. J. Hydrogen Energy* **1998**, *23*, 247–252.

(29) Zhu, Y.; Zhang, X.; Song, J.; Wang, W.; Yue, F.; Ma, Q. Microstructure and Hydrogen Evolution Catalytic Properties of Ni-Sn Alloys Prepared by Electrodeposition Method. *Appl. Catal. A Gen.* **2015**, *500*, 51–57.

(30) Kubisztal, J.; Budniok, A. Study of the Oxygen Evolution Reaction on Nickel-Based Composite Coatings in Alkaline Media. *Int. J. Hydrogen Energy* **2008**, *33*, 4488–4494.

(31) Zhu, Y.; Liu, T.; Li, L.; Song, S.; Ding, R. Nickel-Based Electrodes as Catalysts for Hydrogen Evolution Reaction in Alkaline Media. *Ionics* **2017**, 1121–1127.

(32) González-Buch, C.; Herraiz-Cardona, I.; Ortega, E.; García-Antón, J.; Pérez-Herranz, V. Study of the Catalytic Activity of 3D Macroporous Ni and NiMo Cathodes for Hydrogen Production by Alkaline Water Electrolysis. *J. Appl. Electrochem.* **2016**, *46*, 791–803.

(33) Lu, X.; Zhao, C. Electrodeposition of Hierarchically Structured Three-Dimensional Nickel–Iron Electrodes for Efficient Oxygen Evolution at High Current Densities. *Nat. Commun.* **2015**, *6*, 1–7.

(34) Putz, M. V.; Mirica, M. C. *Sustainable Nanosystems Development, Properties, and Applications*; IGI Global, 2016; pp 370.

(35) Zach, M. P.; Penner, R. M. Nanocrystalline Nickel Nanoparticles. *Adv. Mater.* **2000**, *12*, 878–883.

(36) Klaus, S.; Cai, Y.; Louie, M. W.; Trotochaud, L.; Bell, A. T. Effects of Fe Electrolyte Impurities on $Ni(OH)_2$/NiOOH Structure and Oxygen Evolution Activity. *J. Phys. Chem. C* **2015**, *119*, 7243–7254.

(37) Sengupta, S.; Patra, A.; Jena, S.; Das, K.; Das, S. A Study on the Effect of Electrodeposition Parameters on the Morphology of Porous Nickel Electrodeposits. *Metall. Mater. Trans.* **2018**, *49*, 1–18.

(38) Ebrahimi, F.; Bourne, G.; Kelly, M.; Matthews, T. Mechanical Properties of Nanocrystalline Nickel Produced by Electrodeposition. *Nanostructured Mater.* **1999**, *11*, 343–350.

(39) Callister, W.; Rethwisch, D. *Materials Science and Engineering: An Introduction*, 7th ed.; John Wiley & Sons, Inc., 2007; pp 189.

(40) Yip, S. Nanocrystals: The Strongest Size. *Nature* **1998**, *391*, 532–533.

(41) Subbaraman, R.; Tripkovic, D.; Chang, K. C.; Strmcnik, D.; Paulikas, A. P.; Hirunsit, P.; Chan, M.; Greeley, J.; Stamenkovic, V.; Markovic, N. M. Trends in Activity for the Water Electrolyser Reactions on 3d M(Ni,Co,Fe,Mn) Hydr(Oxy)Oxide Catalysts. *Nat. Mater.* **2012**, *11*, 550–557.

(42) Corrigan, D. A. The Catalysis of the Oxygen Evolution Reaction by Iron Impurities in Thin Film Nickel Oxide Electrodes. *J. Electrochem. Soc.* **1987**, *134*, 377–384.

(43) Klaus, S.; Louie, M. W.; Trotochaud, L.; Bell, A. T. Role of Catalyst Preparation on the Electrocatalytic Activity of $Ni_{1-x}Fe_xOOH$ for the Oxygen Evolution Reaction. *J. Phys. Chem. C* **2015**, *119*, 18303–18316.

(44) Low, W.; M. Schieber. *Applied Solid State Physics*; Plenum Press, New York, NY, 1970; pp 451–452.

(45) Childs, K. D. *Handbook of Auger Electron Spectroscopy: A Book of Reference Data for*

*Identification and Interpretation in Auger Electron Spectroscopy*; 3rd Ed.; Physical Electronics, 1996; pp 92–93.

(46) Gerson, A.; Biesinger, M. C.; Smart, R. S. C.; Payne, B. P.; Lau, L. W. M. X-Ray Photoelectron Spectroscopic Chemical State Quantification of Mixed Nickel Metal, Oxide and Hydroxide Systems. *Surf. Interface Anal.* **2009**, *41*, 324–332.

(47) Biesinger, M. C.; Payne, B. P.; Hart, B. R.; Grosvenor, A. P.; McIntryre, N. S.; Lau, L. W.; Smart, R. S. Quantitative Chemical State XPS Analysis of First Row Transition Metals, Oxides and Hydroxides. *J. Phys. Conf. Ser.* **2008**, *100*, 012025.

(48) Trotochaud, L.; Young, S. L.; Ranney, J. K.; Boettcher, S. W. Nickel-Iron Oxyhydroxide Oxygen-Evolution Electrocatalysts: The Role of Intentional and Incidental Iron Incorporation. *J. Am. Chem. Soc.* **2014**, *136*, 6744–6753.

(49) Thangasamy, P.; Maruthapandian, V.; Saraswathy, V.; Sathish, M. Supercritical Fluid Processing for the Synthesis of $NiS_2$ Nanostructures as Efficient Electrocatalysts for Electrochemical Oxygen Evolution Reactions. *Catal. Sci. Technol.* **2017**, *7*, 3591–3597.

(50) Boubatra, M.; Azizi, A.; Schmerber, G.; Dinia, A. The Influence of pH Electrolyte on the Electrochemical Deposition and Properties of Nickel Thin Films. *Ionics* **2012**, *18*, 425–432.

(51) Bard, A. J.; Faulkner, L. R. *Electrochemical Methods: Fundamentals and Applications*; 2nd Ed.; John Wiley & Sons, Inc.: New York, NY, 2015; Vol. 8, pp 28–29.

(52) Gorlin, M.; De Araujo, J. F.; Schmies, H.; Bernsmeier, D.; Dresp, S.; Gliech, M.; Jusys, Z.; Chernev, P.; Kraehnert, R.; Dau, H.; Strasser, P. Tracking Catalyst Redox States and

Reaction Dynamics in Ni-Fe Oxyhydroxide Oxygen Evolution Reaction Electrocatalysts: The Role of Catalyst Support and Electrolyte pH. *J. Am. Chem. Soc.* **2017**, *139*, 2070–2082.

(53) Trotochaud, L.; Ranney, J. K.; Williams, K. N.; Boettcher, S. W. Solution-Cast Metal Oxide Thin Film Electrocatalysts for Oxygen Evolution. *J. Am. Chem. Soc.* **2012**, *134*, 17253–17261.

(54) Zhou, H.; Yu, F.; Sun, J.; He, R.; Chen, S.; Chu, C.-W.; Ren, Z. Highly Active Catalyst Derived from a 3D Foam of $Fe(PO_3)_2/Ni_2P$ for Extremely Efficient Water Oxidation. *Proc. Natl. Acad. Sci.* **2017**, *114*, 5607–5611.

(55) Lu, Z.; Zhu, W.; Yu, X.; Zhang, H.; Li, Y.; Sun, X.; Wang, X.; Wang, H.; Wang, J.; Luo, J.; Lei, X. Ultrahigh Hydrogen Evolution Performance of Under-Water "Superaerophobic" $MoS_2$ Nanostructured Electrodes. *Adv. Mater.* **2014**, *26*, 2683–2687.

(56) Li, J.; Cheng, H. M.; Chan, C. Y.; Ng, P. F.; Chen, L.; Fei, B.; Xin, J. H. Superhydrophilic and Underwater Superoleophobic Mesh Coating for Efficient Oil–Water Separation. *RSC Adv.* **2015**, *5*, 51537–51541.

## TABLE OF CONTENTS GRAPHIC